

WIND TUNNEL TESTING OF WHIRL FLUTTER AEROELASTIC DEMONSTRATOR

Jiří Čečrdle[1], Ondřej Vích[1], Petr Malínek[1], Robert Kulhánek[1]

[1]VZLU AEROSPACE (Czech Aerospace Research Centre), Prague, Czechia

Abstract

Submitted paper discusses the recent accomplishments in the wind tunnel testing of the W-WING whirl flutter demonstrator. First, the paper gives an outline on theoretical background on the whirl flutter phenomenon, the demonstrator itself and past design and development activities. Further, the preparatory experiments including mass and stiffness measurements, modal tests and engine tests are outlined. The main focus is then paid on the wind tunnel measurements that include two measurement campaigns. The paper provides a description of the test equipment and methodology during both campaigns. In addition, the test result assessment methodology and the examples of results are provided. Finally, the outcome and future activities are outlined.

Keywords: flutter, whirl flutter, W-WING, OFELIA project

1. Introduction

Whirl flutter is a specific type of aeroelastic flutter instability, which may appear on turboprop aircraft due to the dynamic and aerodynamic effect of rotating parts, such as a propeller or a gas turbine engine rotor that generate additional forces and moments. In addition, a flow field behind a rotating propeller causes an aerodynamic interference effect between a nacelle and a wing. Whirl flutter may lead to an instability that is driven by motion-induced unsteady aerodynamic propeller forces and moments acting at the propeller plane. As the outcome, whirl flutter instability may cause unstable vibration and even a failure of an engine installation or an entire wing.

The propeller whirl flutter phenomenon was analytically discovered by Taylor and Browne in 1938 [1]. The basic formulae for the aerodynamic derivatives of propeller forces and moments due to the motion and velocities in pitch and yaw were set by Ribner in 1945 [2, 3]. The importance of the whirl flutter phenomenon on practical applications was recognized after the fatal accidents of two Lockheed L-188 C Electra II airliners in 1959 and 1960 [4].

Due to the complicated physical principle of the whirl flutter, the experimental validation of analytical results is required. The main reasons are the unreliable analytical solution of propeller aerodynamic forces and also a structural damping on which whirl flutter is extremely sensitive. Therefore, aeroelastic models are used. The comprehensive experimental works were carried out in NASA LARC by Reed, Bennett, Kvaternik and many others [5 - 10]. Other important works on the subject are also reported in [11]. A comprehensive description of whirl flutter experimental research activities during the various periods is provided in [12].

The activities of the recent past include the experimental works accomplished by VZLU using the W-WING whirl flutter aeroelastic demonstrator [13]. The demonstrator is based on the aeroelastic model of a turboprop aircraft that was formerly used for certification purposes and for the research of nonlinearities [14, 15]. The developed whirl flutter research demonstrator represents the half-wing and engine of a typical commuter turboprop aircraft structure with a powered rotating propeller. The previously accomplished experimental works are documented e.g. in [16, 17].

2. Description of W-WING Demonstrator

2.1 Mechanical Concept

Whirl flutter aeroelastic demonstrator (W-WING) was adapted from a half-wing with a span of 2.56 m with the engine of a former aeroelastic model of the commuter aircraft for 40 passengers. The total mass of the model (including the simulation of the full fuel load) is approximately 55 kg (wing 30 kg and nacelle 25 kg). Based on the experience from the past activities accomplished within the past project in 2014 and 2015, design modifications and further upgrades were proposed [18]. The main change is the installation of the new motor with sufficient power. Also, additional sensors and equipment were installed. In addition, the system of steady and unsteady flow field measurement was designed. Apart from the described configuration, the sting-mounted nacelle variant, i.e., propeller-nacelle only (W-STING) intended for the measurements of propeller aerodynamic derivatives is also available.

The wing and aileron stiffness is modeled by a duralumin spar of variable cross-section. The inertia characteristics are modeled by lead weights. The aileron is actuated by the electromagnetic shaker placed at the wing root via a push-pull rod. The nacelle model has two DOFs (engine pitch and yaw) modeled by means of cross-spring pivots that are independently replaceable to adjust the stiffness and movable in the direction of the propeller axis to adjust the pivot points of both vibration modes. The inertia of the engine is modeled by the movable weight. The gyroscopic effect of the rotating mass is simulated by the mass of the propeller blades. The propeller is powered by an electric motor with a nominal power of 15 kW. Such power enables to provide the measurement in the thrusted propeller conditions. Power system is equipped with a servo-amplifier to manage and evaluate propeller revolutions, torque, and immediate power. In addition, a balance cell for the measurement of the propeller thrust is installed. Demonstrator is equipped with a system of aerodynamic excitation by aileron flapping deflection. The demonstrator installed in the wind tunnel is shown in figure 1.

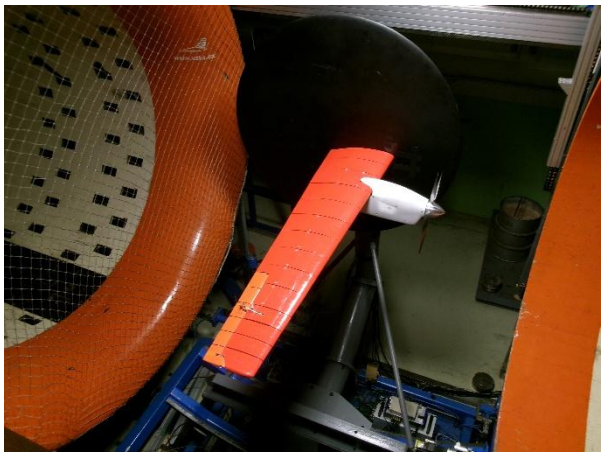


Figure 1 – W-WING research demonstrator.

2.2 Sensor Instrumentation

Mechanical instrumentation includes strain gauges in the root and half-span sections to measure the vertical bending, in-plane bending, and torsional stress of the wing. Demonstrator is also equipped with 18 uniaxial accelerometers. Wing is instrumented at six spanwise sections and two positions chordwise for the vertical direction and at a single position in the wingtip for the in-plane (longitudinal) direction. Nacelle is instrumented in two sections (front and rear) for both vertical and horizontal directions and at the rear section also for the longitudinal direction.

Demonstrator and data control are provided by the in-house LabVIEW-based application. The application provides control of the propeller rotation; propeller rpm may be set either directly or via required thrust. The application also manages aerodynamic excitation by the aileron flapping. Various excitation signals (harmonic constant or sweep, impulse etc.) are available. Measured data from the sensors are acquired with the sampling frequency of 2000 Hz and depicted in the time domain as well as pre-processed into the form of power spectral densities. Finally, the application provides a safeguard preventing the destruction of the demonstrator, provided the response at the critical points exceeds the preset threshold. Apart from the described application, continuous signals from all accelerometers and the airflow velocity signal are acquired using the LMS TestLab system that provides the amplitude evolution and the monitoring of the frequency components corresponding to the engine whirl motion in real-time. Finally, the acquired data are used for the assessment of the demonstrator's vibration response using the methods of FFT and OMA.

3. Ground Tests

Ground tests were aimed at determining the static and dynamic characteristics of the demonstrator and the operational limits of the power system.

3.1 Nacelle Component Tests

The nacelle component tests included stiffness tests to obtain effective stiffness in pitch and yaw directions and modal tests to obtain engine pitch and yaw frequencies. These tests included all five variants of cross spring pivot leaves thickness. A simple system of incremental sensors and loading by weights was used for the static tests. For the modal test, the modal hammer excitation was used. Nacelle component tests are documented in figure 2.



Figure 2 – Nacelle component tests, (a) vertical stiffness test, (b) horizontal stiffness test (loading), (c) modal test (excitation).

3.2 Complete Model Tests

Complete model tests were aimed at determining the modal characteristics of the complete model, i.e., including the wing modes for a single (nominal) configuration. The tests included ordinary modal tests without rotation of the propeller and operational modal analysis (OMA) under the conditions of the rotating propeller at 1000, 2000 and 3000 rpm with the blades' angle of attack of 5, 10 and 15 degrees. In addition, the measurement using the mass equivalent disc was performed. The purpose was to describe the effect of the propeller rotation onto modal parameters and to split the effect of aerodynamic and dynamic forces. Complete model modal test arrangement is shown in figure 3.



Figure 3 – Complete model tests, (a) modal tests layout, (b) mass equivalent disc configuration.

Example of the OMA results is presented in figure 4 that represents cross-power spectra at angle of attack 5 deg and rpm = 1000. Presented curves represent the accelerometer sensors (nacelle or wing).

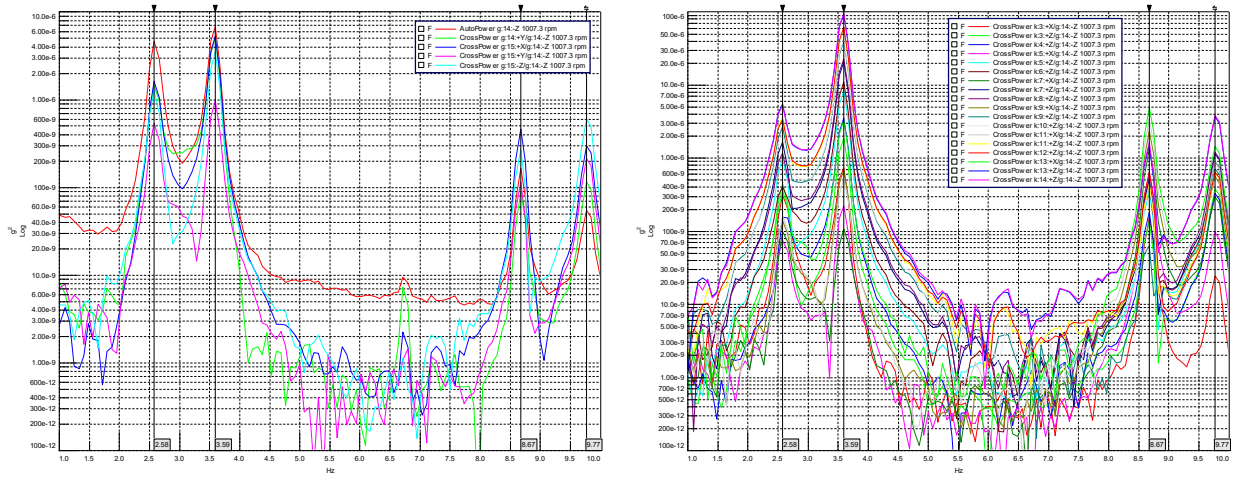


Figure 4 – OMA result example, cross-power spectra, AoA = 5 deg, rpm = 1000, (a) nacelle sensors, (b) wing sensors.

3.3 Power Plant Operational Tests

Power plant operation tests were performed to check the operational envelope of the power system and to find the maximal available revolutions for various angles of attack with respect to the available power. Also, other power plant-related quantities were monitored. The tests included angle of attack

of 5, 10 and 15 degrees. Figure 5 shows the resulting diagrams of the propeller thrust and immediate power vs. propeller rpm.

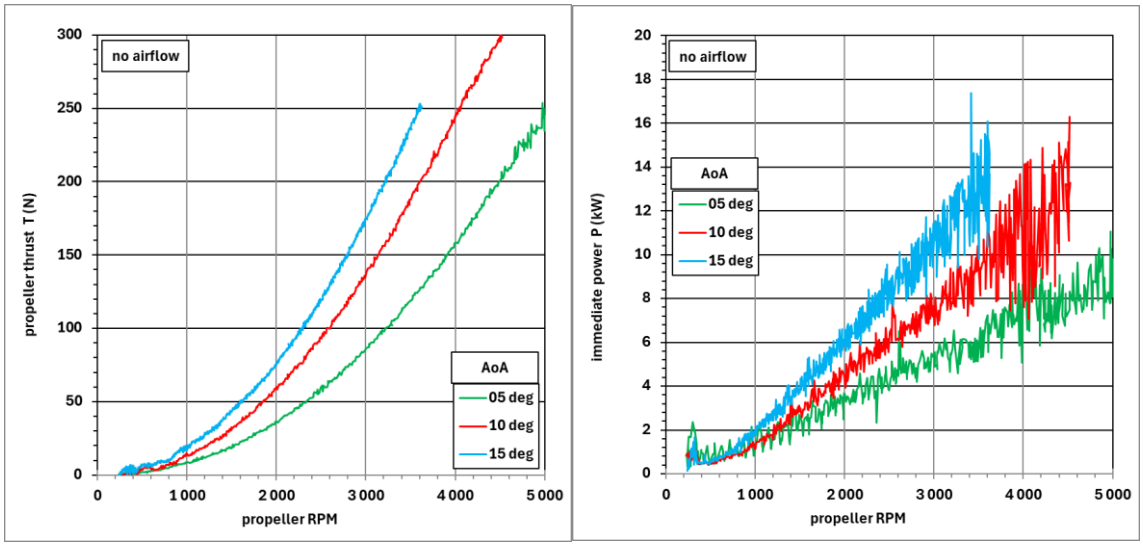


Figure 5 – Power system operational tests, (a) thrust vs. rpm, (b) immediate power vs. rpm.

Considering the expected time of a measurement run and the heat-related motor limitations, the maximal applicable operational power was expected at 10 to 11 kW. From this value, the maximal applicable rpm can be predicted.

4. Wind Tunnel Tests

4.1 Test Arrangement and Methodology

The demonstrator is designed for testing in the VZLU 3-m diameter low-speed wind tunnel. Two campaigns aimed at dynamic response and whirl flutter measurements were accomplished. The demonstrator, combined with the splitter plate which prevents the induced effects at the wing root region, was fixed to the attachment arm inside the wind tunnel test section as shown in figure 6.

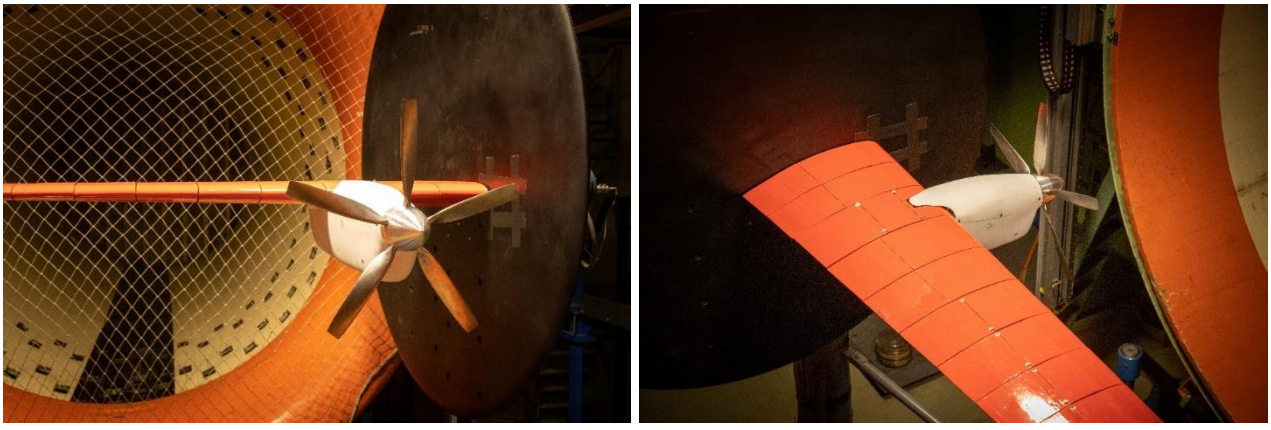


Figure 6 – Wind tunnel test arrangement.

The measurement variant was defined by these structural parameters: pitch and yaw attachment stiffness, pitch and yaw hinge station, balance weight station, choice of propeller (duralumin or steel blades), and finally, by the propeller blade 75% section angle of attack (α). The measurement of each variant included the preparatory measurement of the pitch and yaw frequencies without the airflow. The reason was that the pitch and yaw effective stiffness were influenced also by the

conditions of assembly. Next, the main measurement including the airflow was performed. In the first phase, the excitation was realized by the flow turbulence only. Provided that no flutter state was reached, the measurement was repeated with excitation by the aileron harmonic sweep flapping. The duration of mechanical measurement at a single velocity was approximately 5 minutes, after steady airflow velocity and the propeller revolutions were reached.

The typical examples of results are shown in the following figures. Figure 7 shows the example of power spectra results for excitation by the airflow turbulence. The graphs represent g-amplitude including both backward and forward whirl modes at the airflow velocities ranging from 10 to 40 m/s.

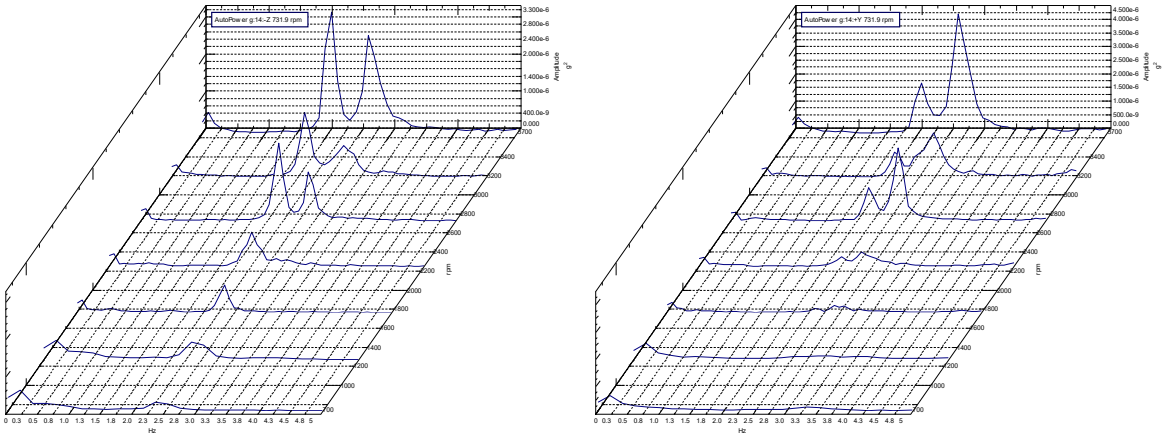


Figure 7 – Power spectra results, turbulence excitation, backward and forward whirl modes, g-amplitude response: (a) pitch and (b) yaw, airflow velocities 10, 15, 20, 25, 30, 35 and 40 m/s.

Figure 8 presents the waterfall diagram for the measurement with excitation by the aileron flapping. The diagram shows the g-amplitude response in the pitch direction at the airflow of 20, 30 and 40 m/s. The highlighted sections are those ones in which the maximal response of the backward (blue) and forward whirl (purple), respectively were reached.

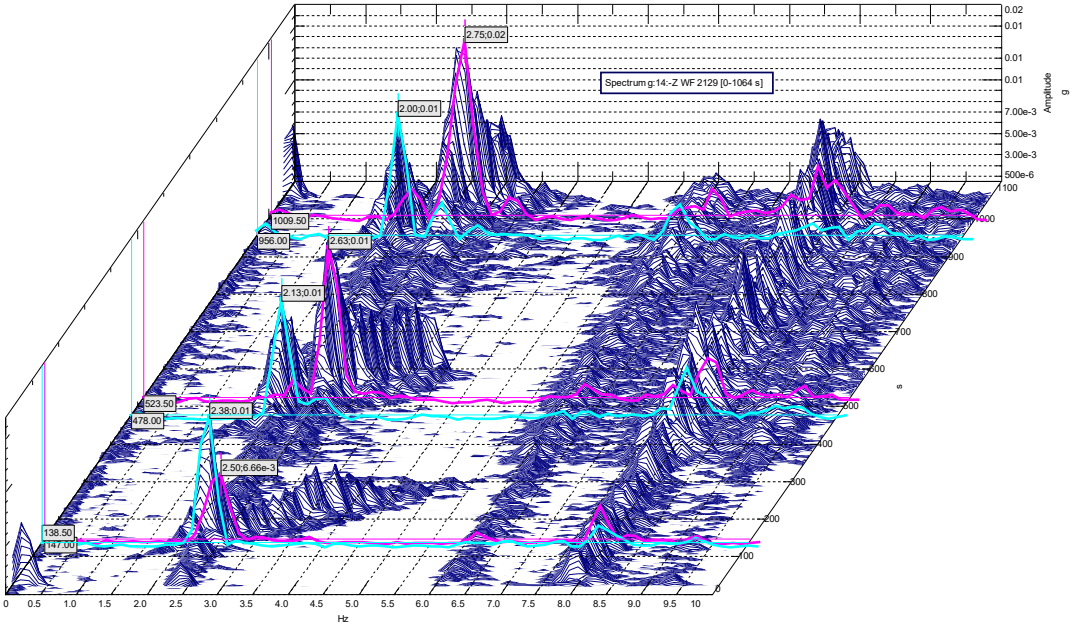


Figure 8 – Waterfall response results, aileron excitation, rpm = 3647, g-amplitude response in pitch direction, airflow velocities 20, 30 and 40 m/s.

The highlighted sections are further presented in figure 9 that includes the g-response in both pitch and yaw directions for the cases in which the maximal response of the backward and forward whirl, respectively were reached. From the figures we can observe the trajectories of both whirl modes. For the backward whirl the trajectory is almost circular with the slightly dominating pitch direction.

For the forward whirl the trajectory is elliptical with the dominating yaw direction.

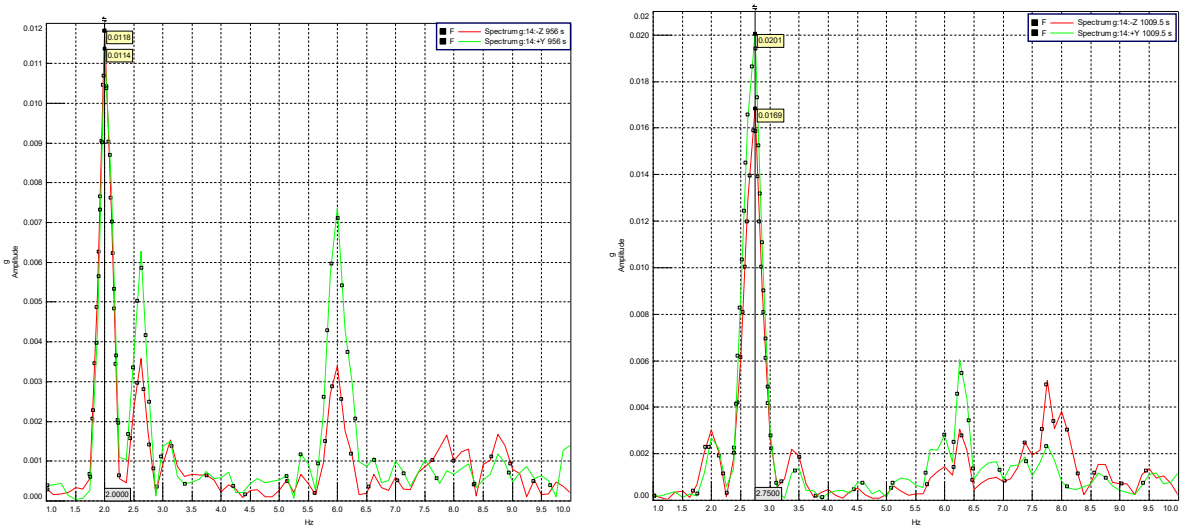


Figure 9 – g-response results, aileron excitation, rpm = 3647, pitch (red) and yaw (green) directions, airflow velocity 40 m/s, (a) maximal backward whirl response and (b) maximal forward whirl response.

Vibrational response data were acquired and processed using FFT. The spectra were sorted by the time and displayed as cascade graphs in the broad frequency range. A detailed assessment in the frequency domain was focused on the frequency range from 0 to 20 Hz. Further, the averaged Cross Power and Auto Power spectra of vibrations were evaluated at the measured points. The data of the runs with the turbulence excitation were the input into the OP Time MDOF algorithm for the operational modal analysis (OMA). The results included modal parameters (frequency, mode shape, damping ratio) of the evaluated modes at the airflow velocities. The identified modes included both backward and forward whirl modes as well as the wing modes, especially 1st bending mode.

4.2 1st Measurement Campaign

During the 1st campaign, the measurement scenario was defined as the fixed-rpm and variable airflow. In this scenario, the propeller rpm is maintained constant while the airflow is increased. However, no flutter state was reached during the measurements. The reason was the influence of the thrust. For the fixed-rpm scenario, the damping may increase due to the decrease in thrust as the airflow increased. The example of such result (V-g-f diagram) is shown in figure 10. It can be observed from the figure the decrease in the damping of backward whirl up to the airflow velocity of 20 m/s. Then, for the higher airflow velocities, the damping starts to increase back due to the decrease in thrust. Apart of the fixed-rpm thrusted propeller regimes, the windmilling propeller measurements were realised as well. Tested variants included a single choice of both pitch and yaw stiffness, two choices of both pitch and yaw pivot stations (front and rear), two choices of the weight station (front and rear), two choices of the propeller blades (duralumin and steel) and two choices of the propeller blades' angle of attack (5 and 10 deg). The described choices of parameters form 16 variants in total. For each variant, the measurements included propeller in the windmilling mode and in thrusted mode with rpm of 3600, 4000 and 4400. Measurement was performed with excitation by the airflow turbulence and by the aileron flapping frequency sweep. Thus, 128 measurement runs in total were done. The typical velocity array for the excitation by the airflow turbulence was 10, 15, 20, 25, 30, 35 and 40 m/s unless the flutter state would have been reached, or the negative thrust was reached for the thrusted mode. Similarly, the airflow velocity array for the excitation by the aileron flapping was 20, 30 and 40 m/s. In the case of approaching a flutter state, the velocity step would have been properly decreased.

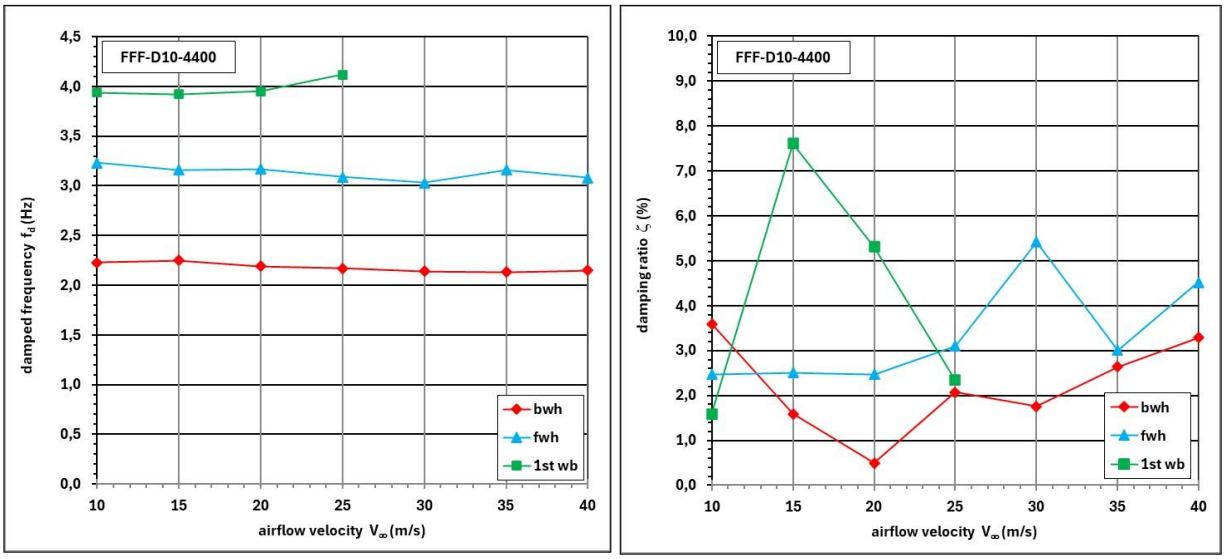


Figure 10 – V-g-f diagram, 1st campaign, fixed-rpm scenario, rpm = 4400, pivots and weight front, duralumin blades, AoA = 10 deg, backward whirl (red), forward whirl (blue) and 1st wing bending (green) modes.

4.3 2nd Measurement Campaign

Based on the above-described experience, the measurement scenario was changed to fixed-thrust and variable airflow during the 2nd campaign. In this scenario, the propeller rpm is controlled to reach the preselected thrust while the airflow is increased. In practice, after the reaching the target thrust, the rpm was locked, and the measurement was started. In this scenario, the rpm is increasing with the airflow velocity and the influence of the thrust on the flutter stability is eliminated. Apart of the fixed-thrust propeller regimes, the windmilling propeller measurements were realised as well. Tested variants included a single choice of both pitch and yaw stiffness, two choices of pitch and yaw pivot and weight stations (front and rear), two choices of the propeller blades (duralumin and steel) and two choices of the propeller blades' angle of attack. For the fixed-thrust regimes, the measured variants included the thrust of 50, 100 and 150 N for the blade angle of attack of 10 deg, and 20 and 50 N for the blade angle of attack of 5 deg. The thrust values were determined according to the values measured during the first campaign to be able to reach the target thrust up to propeller rpm of 5000 at the reasonable range of the airflow velocities. Another condition was the limit engine temperature to prevent over-heat considering the duration of a single run including both vibrational response and aerodynamic flow field measurements (see chapter 4.4) that was approximately 30 mins. Due to this factor, the applicable engine power was limited by the value of approximately 8 kW. Similarly to the first campaign, the excitation included the airflow turbulence and the excitation by the aileron flapping frequency sweep. Airflow velocity array for the excitation by the airflow turbulence was 10, 15, 20, 25, 30, 35 and 40 m/s unless the flutter state has been reached or the required propeller rpm to reach the target thrust exceeded the maximal applicable value of 5000. Similarly, the airflow velocity array for the excitation by the aileron flapping was 20, 30 (optionally 25) and possibly also 40 m/s. In the case of approaching a flutter state, the velocity step was properly decreased. A minimal velocity step of 1 m/s was used. The measurements with the windmilling propeller were performed similarly. For the fixed-thrust regimes, the measurement run included just a single velocity to avoid the engine over-heating considering the duration of the measurement that included both the vibrational response measurement and aerodynamic flow field measurement (see chapter 4.4). The measurements with the excitation by the aileron and the windmilling regimes were performed at a single run including the multiple airflow velocities as these cases included the mechanical measurements only.

Figure 11 shows V-g-f diagram for the case in which the flutter state was reached. Unstable response was found at V = 29 and 30 m/s. Note that the positive damping was evaluated using OMA while the

negative damping was evaluated using logarithmic decrement. Also, the reduced velocity step applied at the flutter-approaching area can be observed.

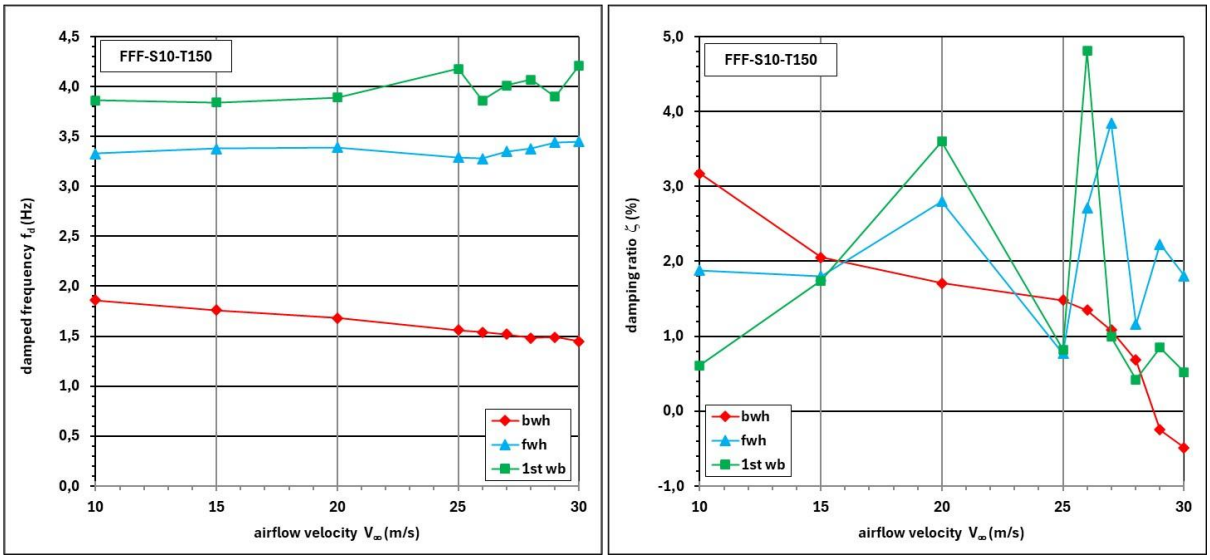


Figure 11 – V-g-f diagram, 2nd campaign, fixed-thrust scenario, T = 150 N, pivots and weight front, steel blades, AoA = 10 deg, backward whirl (red), forward whirl (blue) and 1st wing bending (green) modes.

The influence of thrust on the flutter stability is documented in figures 12 to 14 that show the rpm, frequency and damping curves of the backward whirl mode over the airflow velocity for three values of thrust (T = 50, 100 and 150 N). For T = 50 N, flutter state has not been reached up to 40 m/s while for T = 100 and 150 N, flutter speed was found at V = 35 and 29 m/s, respectively. Note that the positive damping (green curve) was evaluated using OMA while the negative damping (red curve and blue symbols) was evaluated using logarithmic decrement. Also, the reduced velocity step applied at the flutter-approaching area can be observed.

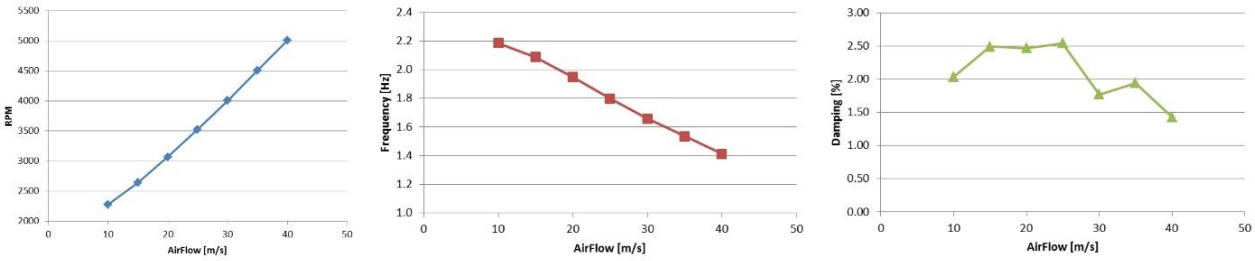


Figure 12 – Backward whirl mode, (a) rpm, (b) frequency and (c) damping curves over airflow velocity, fixed-thrust scenario, T = 50 N, pivots and weight front, steel blades, AoA = 10 deg, no flutter state reached.

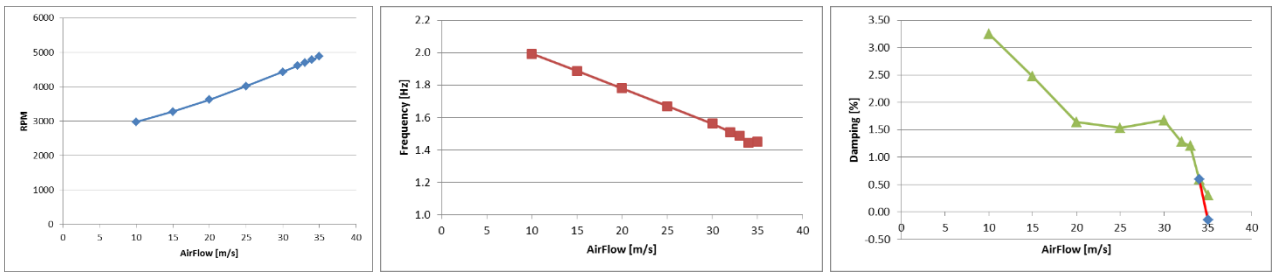


Figure 13 – Backward whirl mode, (a) rpm, (b) frequency and (c) damping curves over airflow velocity, fixed-thrust scenario, T = 100 N, pivots and weight front, steel blades, AoA = 10 deg, V_{FL} = 34 m/s.

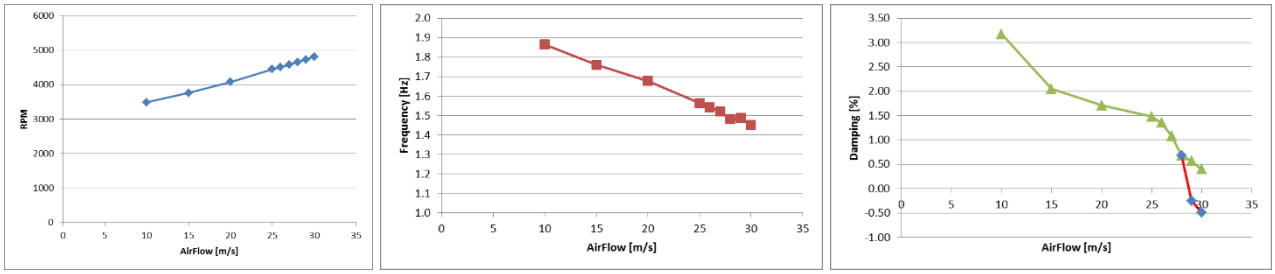


Figure 14 – Backward whirl mode, (a) rpm, (b) frequency and (c) damping curves over airflow velocity, fixed-thrust scenario, T = 150 N, pivots and weight front, steel blades, AoA = 10 deg, V_{FL} = 29 m/s.

Flutter state was defined using g-response criterion (0.05 g) measured at the nacelle front section. The value was set to ensure the structural integrity of the demonstrator with respect to the expected flutter frequency (1.4 to 1.5 Hz). Figure 15 shows the record of the mm-amplitude in pitch and yaw directions until the flutter criterion was reached.

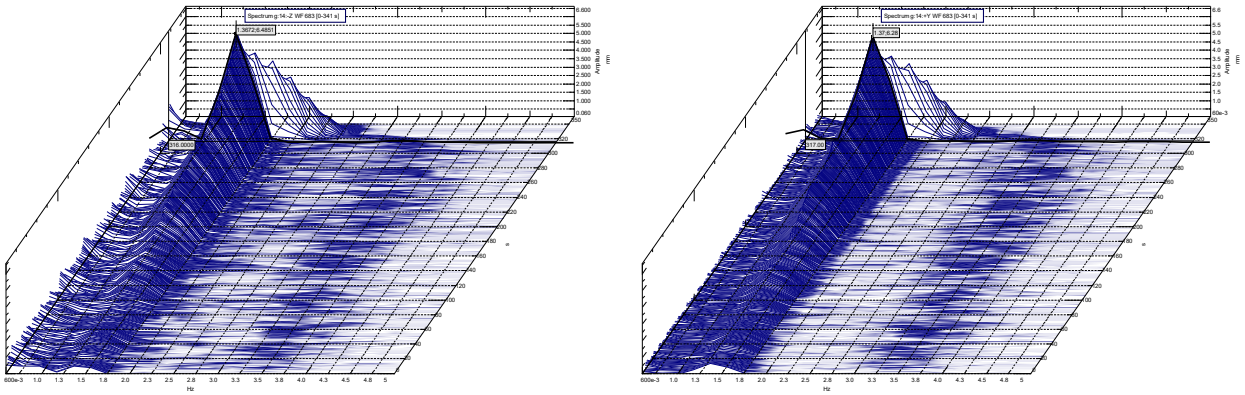


Figure 15 – Amplitude (mm) at nacelle front sensor section, (a) pitch, (b) yaw, fixed-thrust scenario, T = 100 N, pivots and weight front, steel blades, AoA = 10 deg, V = 34 m/s

Finally, the evolution of the maximal measured g-amplitude at the nacelle front section over the airflow velocity can be observed from figure 16.

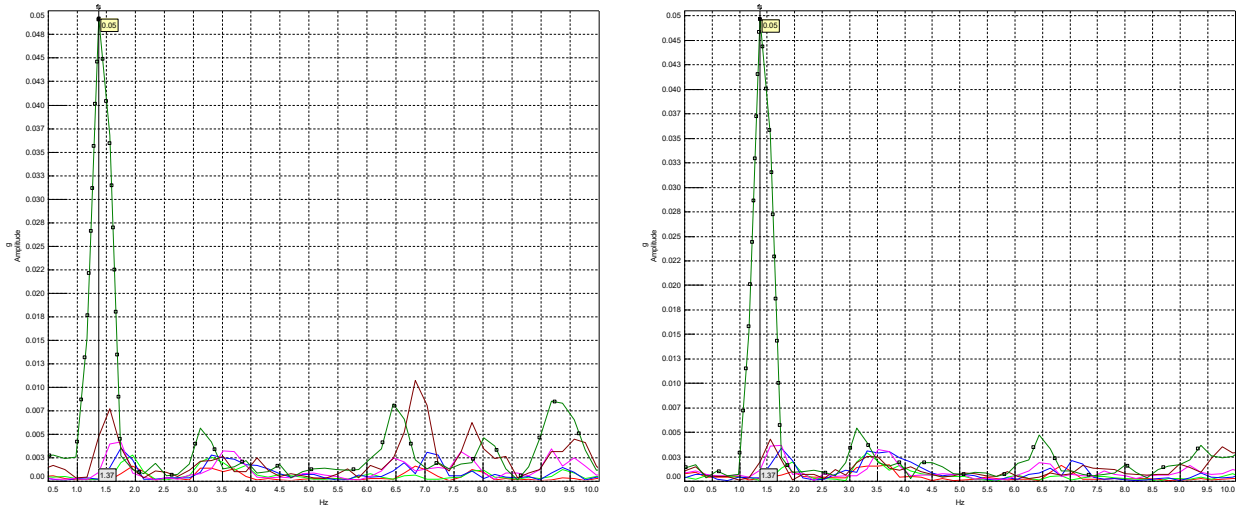


Figure 16 – Maximal amplitude (g) at nacelle front sensor section, (a) pitch, (b) yaw, fixed-thrust scenario, T = 100 N, pivots and weight front, steel blades, AoA = 10 deg, parameter – airflow velocity: red: 10 m/s, 2973 rpm, green: 15 m/s, 3275 rpm, blue: 20 m/s, 3627 rpm, purple: 25 m/s, 4015 rpm, brown: 30 m/s, 4453 rpm and dark-green: 35 m/s, 4640 rpm.

4.4 Aerodynamic Flow-field Measurement

In addition to the above-described mechanical measurements, the aerodynamic flow-field measurements were performed during the 2nd measurement campaign. Measurements included the steady measurement using five-hole pressure probe and the unsteady measurement using hot-wire anemometer probe. Both ones were attached to the common manipulation arm as shown in figure 17.

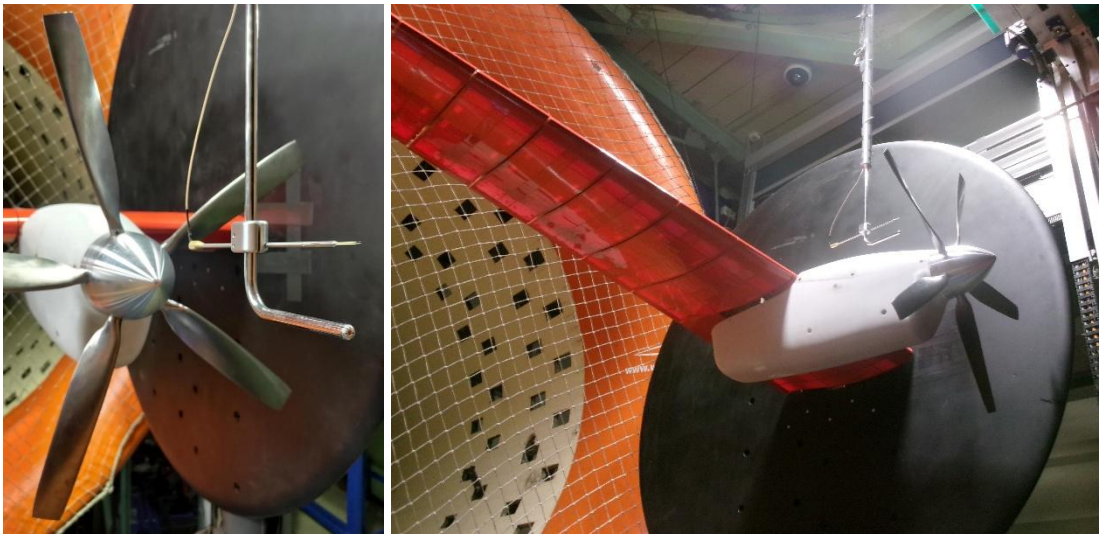


Figure 17 – Installation of aerodynamic flow-field measurement probes.

Measurements were performed at the defined points around the nacelle, propeller and wing as shown in figure 18. The aerodynamic measurement was realised after the mechanical measurements with the turbulence excitation sequentially point by point. Obviously, it was not feasible to make this measurement in the cases of approaching a flutter state. The aerodynamic measurement was realised only provided that the structural response was considered as stable. As the results of steady measurements, the velocity magnitudes and pitch and yaw angles were evaluated. As the results of the unsteady measurements the phase averaged velocities and turbulence intensities over the propeller azimuth angle were evaluated.

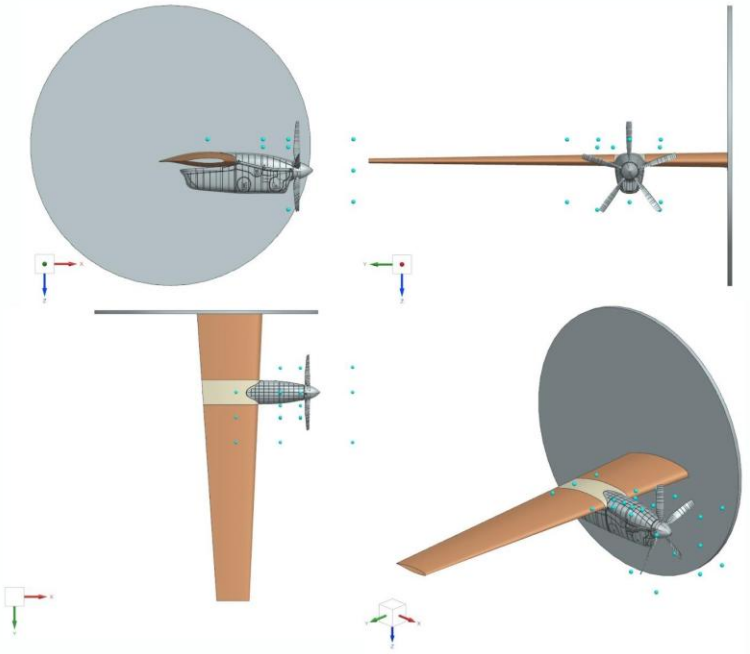


Figure 18 – Grid of measured points for aerodynamic flow-field measurement.

The example of the steady aerodynamic flow field measurement is shown in figure 19. The figure represents the velocity profile behind the propeller at the airflow velocity of 10 m/s and three levels of the propeller rpm (2400, 2940 and 3670). The velocity magnitude increase can be observed behind the propeller up to r ~ 280 mm while the velocity magnitude decrease can be observed at the propeller tip part. Also, an increase in the pitch direction angle can be observed at the propeller tip part. Note that the propeller radius is 350 mm and r = 0 represents the propeller axis.

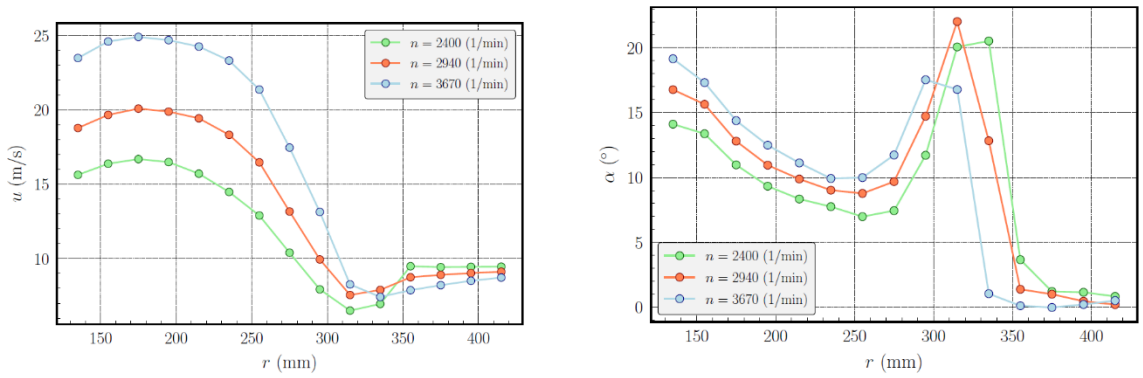


Figure 19 – Steady aerodynamic measurement, velocity profile behind propeller, V = 10 m/s, parameter: propeller rpm, (a) velocity magnitude, (b) pitch angle.

The example of unsteady aerodynamic measurement results is shown in figure 20. The figure represents the averaged velocity magnitude and turbulence intensity at a point behind the propeller over the propeller revolution at the airflow velocity of 10 m/s. Note that the propeller has five blades. Thus, five velocity magnitude and turbulence intensity peaks can be observed from the figure. These peaks represent the local increase passing through the propeller blades.

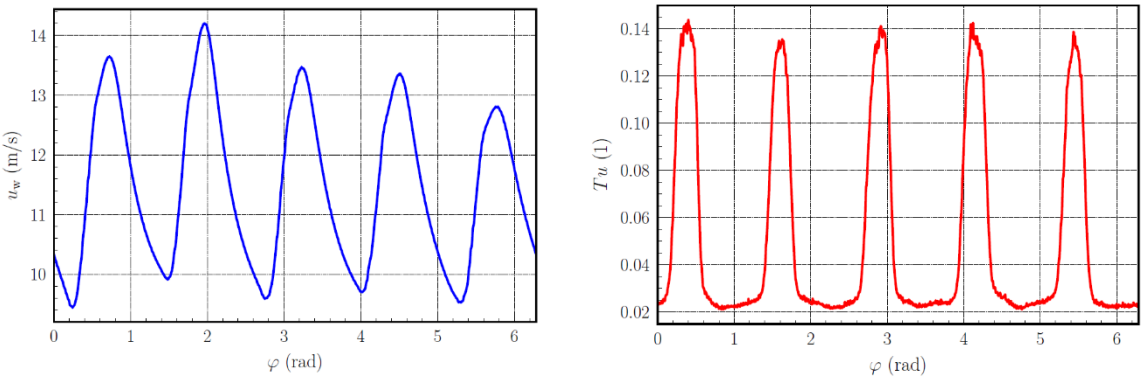


Figure 20 – Unsteady aerodynamic measurement, velocity behind propeller over a propeller revolution, V = 10 m/s, (a) velocity magnitude, (b) turbulence intensity.

5. Conclusion and Outlook

Submitted paper discusses the recent accomplishments in the wind tunnel testing of the W-WING whirl flutter demonstrator. Two experimental campaigns were accomplished within the subject project. The tests include mechanical measurements (aeroelastic response and flutter states) as well as aerodynamic flow field measurements (steady and unsteady). The experimental results obtained will be subsequently utilized for verification of the analytical models and computational tools [20 – 22] that will be used for development of the new power plant system characterized as an open-fan concept utilized for a new generation short-medium range turboprop aircraft.

6. Acknowledgements

Program and topic: HORIZON-JU-CLEAN-AVIATION-2022-01-SMR-01, Ultra Efficient Propulsion Systems for Short and Short-Medium Range Aircraft. Project nr. and title: 101102011, Open Fan for Environmental Low Impact of Aviation (OFELIA).

Other contributing people of the VZLU project team: Jan Červinka, Radek Doubrava, Erik Flídr, Miroslav Golda, Michal Havel, Miloš Chvátal, Miloš Javůrek, Tomáš Jelínek, Václav Klouda, Zuzana Lašová, Vladimír Muller, David Novotný, Jan Raška, Jan Stárek, Václav Strnad, Miroslav Šmíd, Jarmil Vlach and Petr Vrchota.

7. Disclaimer

Funded by the European Union. Views and opinions expressed are however those of the author(s) only and do not necessarily reflect those of the European Union or the Clean Aviation Joint Undertaking. Neither the European Union nor the granting authority can be held responsible for them.

8. Contact Author Email Address

mailto: cecrdle@vzlu.cz

9. Copyright Statement

The authors confirm that they, and/or their company or organization, hold copyright on all of the original material included in this paper. The authors also confirm that they have obtained permission, from the copyright holder of any third-party material included in this paper, to publish it as part of their paper. The authors confirm that they give permission or have obtained permission from the copyright holder of this paper, for the publication and distribution of this paper as part of the ICAS proceedings or as individual off-prints from the proceedings.

References

[1] Taylor, E. S., and Browne, K. A. Vibration Isolation of Aircraft Power Plants, *J. Aerosp. Sci.*, 6(2):43-49, 1938.

[2] Ribner, H. S. *Propellers in Yaw*, NACA, Report 820, 1945.

[3] Ribner, H. S. *Formulas for Propellers in Yaw and Charts of the Side - Force Derivatives*, NACA, Report 819, 1945.

[4] Donham, R. E. and Watts, G. A. Whirl Flutter First Case, *In: The Revolution in Structural Dynamics, (Editor Dr. Hugh Flomenhoft)*, Dynaflo Press, Palm Beach Gardens, FL, USA, 99-109, 1997.

[5] Reed, W. H. and Bland, S. R. *An Analytical Treatment of Aircraft Propeller Precession Instability*, NASA, TN D-659, 1961.

[6] Reed, W. H. and Bennett, R. M. Propeller Whirl Flutter Considerations for V/STOL Aircraft, *In: CAL/TRECOM Symposium*, Buffalo, NY, USA, 1963.

[7] Bland, S. R. and Bennett, R. M. *Wind-Tunnel Measurement of Propeller Whirl-Flutter Speeds and Static Stability Derivatives and Comparison with Theory*, NASA, TN D-1807, 1963.

[8] Bennett, R. M. and Bland, S. R. *Experimental and Analytical Investigation of Propeller Whirl Flutter of a Power Plant on a Flexible Wing*, NASA, TN D-2399, 1964.

[9] Abbott, F.T., Jr., Kelly, H. N. and Hampton, K. D. *Investigation of Propeller-Power Plant Autoprecession*

Boundaries for a Dynamic-Aeroelastic Model of a Four-Engine Turboprop Transport Airplane, NASA, TN D-1806, 1963.

[10] Kvaternik, R. G. and Kohn, J. S. *An Experimental and Analytical Investigation of Proprotor Whirl Flutter*, NASA, TP 1047, 1977.

[11] Krishna Rao, K. V. and Sundararajan, D. *Whirl Flutter of Flapping Blade Rotor Systems*, National Aeronautical Laboratory, Bangalore, India, TN-18, 1969.

[12] Čečrdle, J. *Whirl Flutter of Turboprop Aircraft Structures*, 2nd Ed., Elsevier Science, Oxford, UK, 2023.

[13] Čečrdle, J. and Maleček, J. Mechanical Concept of W-WING Whirl Flutter Aeroelastic Demonstrator, *Proc. Institution of Mech. Engineers, Part G: J. Aerosp. Eng*., 229(8):1485-1494, 2013.

[14] Maleček, J., Hlavatý, V., Malínek, P. and Čečrdle, J. Development of Wing / Engine Component Non-linear Aeroelastic Demonstrator, *In: International Forum on Aeroelasticity and Structural Dynamics*, Paris, France, 2011.

[15] Maleček, J., Čečrdle, J., Hlavatý, V. and Malínek, P. Mechanical Concepts for Simulation of Nonlinearities on Aeroelastic Demonstrator, *J. Aircr.*, 50(2):651-658, 2013.

[16] Čečrdle, J., Malínek, P. and Vích, O. Wind Tunnel Test of a Whirl Flutter Aeroelastic Demonstrator, *In: Proc. AIAA SciTech Forum*, San Diego, CA, USA, 2017.

[17] Čečrdle, J., Vích, O. and Malínek, P. Wind Tunnel Test of a Whirl Flutter Aeroelastic Demonstrator, *Proc. Institution of Mech. Engineers, Part G: J. Aerosp. Eng*., 233(3):969-977, 2019.

[18] Čečrdle, J., Vích, O., Stárek, J., Vlach, J., Kolář, M. and Šmíd, M. W-WING Aeroelastic Demonstrator Design Modification and Upgrade, *In.: Congress of the International Council of the Aeronautical Sciences,* Florence, Italy, 2024.

[19] Houbolt, J. C. and Reed, W. H. Propeller Nacelle Whirl Flutter, *J. Aerosp. Sci.*, 29:333-346, 1962.

[20] Dugeai, A., Mauffrey, Y. and Sicot, F. Aeroelastic Capabilities of the elsA Solver for Rotating Machines Applications, *In: Int. Forum on Aeroelasticity and Structural Dynamics*, Paris, France, 2011.

[21] Sicot, F. and Dugeai, A. Numerical Investigation of Propellers Whirl Flutter Using elsA, *In: Int. Forum on Aeroelasticity and Structural Dynamics*, Paris, France, 2011.

[22] Placzek, A., Riols-Fonclare A., Dugeai, A., Liauzun, C., Blondeau, C. and Des Boscs, P. E. Towards Modular Aeroelastic Simulations: Recent Developments and Applications at ONERA, *In: Int. Forum on Aeroelasticity and Structural Dynamics*, The Hague, The Netherlands, 2024.